

Article

Two Novel C₃N₄ Phases: Structural, Mechanical and Electronic Properties

Qingyang Fan ^{1,*}, Changchun Chai ¹, Qun Wei ² and Yintang Yang ¹

¹ Key Laboratory of Ministry of Education for Wide Band-Gap Semiconductor Materials and Devices, School of Microelectronics, Xidian University, Xi'an 710071, China; ccchai@mail.xidian.edu.cn (C.C.); ytyang@xidian.edu.cn (Y.Y.)

² School of Physics and Optoelectronic Engineering, Xidian University, Xi'an 710071, China; qunwei@xidian.edu.cn

* Correspondence: fanqy1991@stu.xidian.edu.cn; Tel.: +86-29-8820-2507

Academic Editor: Martin O. Steinhauser

Received: 26 April 2016; Accepted: 24 May 2016; Published: 30 May 2016

Abstract: We systematically studied the physical properties of a novel superhard (*t*-C₃N₄) and a novel hard (*m*-C₃N₄) C₃N₄ allotrope. Detailed theoretical studies of the structural properties, elastic properties, density of states, and mechanical properties of these two C₃N₄ phases were carried out using first-principles calculations. The calculated elastic constants and the hardness revealed that *t*-C₃N₄ is ultra-incompressible and superhard, with a high bulk modulus of 375 GPa and a high hardness of 80 GPa. *m*-C₃N₄ and *t*-C₃N₄ both exhibit large anisotropy with respect to Poisson's ratio, shear modulus, and Young's modulus. Moreover, *m*-C₃N₄ is a quasi-direct-bandgap semiconductor, with a band gap of 4.522 eV, and *t*-C₃N₄ is also a quasi-direct-bandgap semiconductor, with a band gap of 4.210 eV, with the HSE06 functional.

Keywords: C₃N₄ allotropes; mechanical properties; electronic properties; superhard materials

1. Introduction

Studies on light element-based materials trace back to the middle of the last century. Since Lavoisier found that diamond was isostructural to carbon and much denser than graphite, many studies have been devoted to its synthesis under high pressure [1–4]. More and more researchers have begun to investigate the carbon allotropes [5–15]. The second light element-based material to be evidenced was boron nitride. It includes three different structures: blende-, wurtzite- and graphitic-type structures. Cubic boron nitride (c-BN) was first elaborated upon in 1957 by Wentorf, who performed direct conversion using graphitic boron nitride (at 7 GPa and 1500 °C) [16]. Many boron nitride allotropes have been investigated by researchers, such as O-BN, Pbca-BN, Z-BN, W-BN, h-BN, bct-BN, P-BN, and cT8-BN. Interest in carbon nitrides has been initiated by studying materials that exhibit mechanical properties comparable with those of diamond. A fullerene is a molecule of carbon in the form of a hollow sphere, ellipsoid, tube, and many other shapes. Gueorguiev *et al.* [17,18] studied the formation mechanisms and structural features of fullerene-like carbon nitride (FL CN_x), utilizing first-principles calculations.

Liu *et al.* first predicted β-C₃N₄ [19]; its structure originated in β-Si₃N₄, with carbon substituting for silicon. In the same way, α-C₃N₄ has been deduced from α-Si₃N₄, replacing silicon with carbon. The bulk of α-C₃N₄ and β-C₃N₄ is 387 and 427 GPa, respectively, which are slightly smaller than that of diamond (431 GPa [20]). Therefore, there are *sp*² and *sp*³ hybridizations on carbon and nitrogen in α-C₃N₄ and β-C₃N₄, respectively. The *pseudocubic*-C₃N₄ structure is isostructural to α-CdIn₂Se₄ [21] and was first proposed by Liu and Wentzcovitch [22]. The network structure of *pseudocubic*-C₃N₄ consists of corners-linked CN₄ tetrahedra in which the C-N-C angle is close to 109°, which ensures *sp*³

hybridization for nitrogen. The bulk modulus of *pseudocubic*-C₃N₄ is 448 GPa, which is slightly larger than that of diamond.

Cubic-C₃N₄ is another C₃N₄ phase and is isostructural to the high-pressure structure of Zn₂SiO₄, which was proposed by Teter and Hemley [23]. The structure of *cubic*-C₃N₄ is similar to that of *pseudocubic*-C₃N₄, including the hybridization. Mo *et al.* [24] and later Kroll [25] proposed a γ -C₃N₄ polymorph derived from a γ -Si₃N₄ spinel high-pressure structure. The largest difference between these structures involves the hybridization of nitrogen and carbon. In *pseudocubic*-C₃N₄ or *cubic*-C₃N₄, both carbon and nitrogen adopt *sp*³ hybridization. *Graphite* C₃N₄ (*g*-C₃N₄) consists of the stacking along the *c*-axis of graphitic planes. Teter and Hemley first described these graphitic planes as a hexagonal organization of C₃N₃ triazine cycles. Because of its graphitic structure, the bulk modulus is only 51 GPa [22,26].

We propose *m*-C₃N₄ (*m* denotes Monoclinic symmetry, space group: Cm) and *t*-C₃N₄ (*t* denotes Tetragonal symmetry, space group: *I*-42*m*), whose structures are based on *m*-Si₃N₄ and *t*-Si₃N₄ [27], respectively, with C substituting for Si. The mechanical and electronic properties of *m*-C₃N₄ and *t*-C₃N₄ are presented in this work.

2. Computational Method

Density functional theory (DFT) [28,29] calculations within Vanderbilt ultrasoft pseudopotentials [30] were performed using the Cambridge Serial Total Energy Package (CASTEP) code [31]. For the exchange and correlation functional, we used the Perdew–Burke–Ernzerhof (PBE) version of the generalized gradient approximation (GGA) [32]. For α -C₃N₄, β -C₃N₄, *d*-ZB-C₃N₄, *Pseudocubic*-C₃N₄, *Cubic*-C₃N₄, *g*-C₃N₄, *m*-C₃N₄ and *t*-C₃N₄, an energy cutoff of 520 eV was used for the wave functions expansion. High dense *k*-point [33] sampling, with a grid spacing of less than $2\pi \times 0.025 \text{ \AA}^{-1}$ ($7 \times 17 \times 9$ for *m*-C₃N₄, $11 \times 11 \times 6$ for *t*-C₃N₄, $12 \times 12 \times 12$ for *d*-ZB-C₃N₄, $12 \times 12 \times 12$ for *pseudocubic*-C₃N₄, $8 \times 8 \times 8$ for *cubic*-C₃N₄, $10 \times 10 \times 6$ for *g*-C₃N₄, $7 \times 7 \times 8$ for α -C₃N₄, and $7 \times 7 \times 18$ for β -C₃N₄) in the Brillouin zone, was used. The equilibrium crystal structures were achieved by utilizing geometry optimization in the Broyden–Fletcher–Goldfarb–Shanno (BFGS) [34] minimization scheme. The self-consistent convergence of the total energy was 5×10^{-6} eV/atom; the maximum force on the atom was 0.01 eV/Å, the maximum ionic displacement was within 5×10^{-4} Å, and the maximum stress was within 0.02 GPa. The electronic properties of *t*-C₃N₄ and *m*-C₃N₄ were calculated using the Heyd–Scuseria–Ernzerhof (HSE06) [35,36] hybrid functional.

3. Results and Discussion

3.1. Structural Properties

The crystal structures of *m*-C₃N₄ and *t*-C₃N₄ are shown in Figure 1. There are 14 (six carbon atoms and eight nitrogen atoms) atoms in a conventional cell of *m*-C₃N₄ and *t*-C₃N₄. Within this structure of *m*-C₃N₄, three inequivalent carbon atoms occupy the (0.8392, 0.0, 0.5479), (0.2917, 0.0, 0.8418) and (0.9864, 0.0, 0.3048) positions, and four inequivalent nitrogen atoms occupy the (0.2050, 0.0, 0.3856), (0.8843, 0.0, 0.8186), (0.3600, 0.0, 0.1253) and (0.5344, 0.5, 0.5771) positions, while for *t*-C₃N₄, two inequivalent carbon atoms occupy the (0.5, 0.5, 0.0) and (0.5, 0.0, 0.75) positions, and nitrogen atoms occupy the (0.7330, 0.2670, 0.8705) position, respectively. The basic building block of *m*-C₃N₄ is the six-membered zigzag carbon-nitrogen rings, which can be clearly observed in Figure 1a; the twelve-membered zigzag carbon-nitrogen rings in the [010] direction in the structure of *m*-C₃N₄ are shown in Figure 1b, while six-membered zigzag carbon-nitrogen rings and eight-membered gauche carbon-nitrogen rings exist in *t*-C₃N₄. The equilibrium lattice parameters of *m*-C₃N₄, *t*-C₃N₄, *d*-ZB-C₃N₄ (space group: *P*-43*m*), *cubic*-C₃N₄ (space group: *I*-43*d*), *pseudocubic*-C₃N₄ (space group: *P*-42*m*), *g*-C₃N₄ (space group: *P*-6*m*2), α -C₃N₄ (space group: *P*31*c*) and β -C₃N₄ (space group: *P*63/*m*) at ambient pressure are listed in Table 1. The calculated parameters of α -C₃N₄ and β -C₃N₄ are in excellent agreement with previous theoretical results (see Table 1).

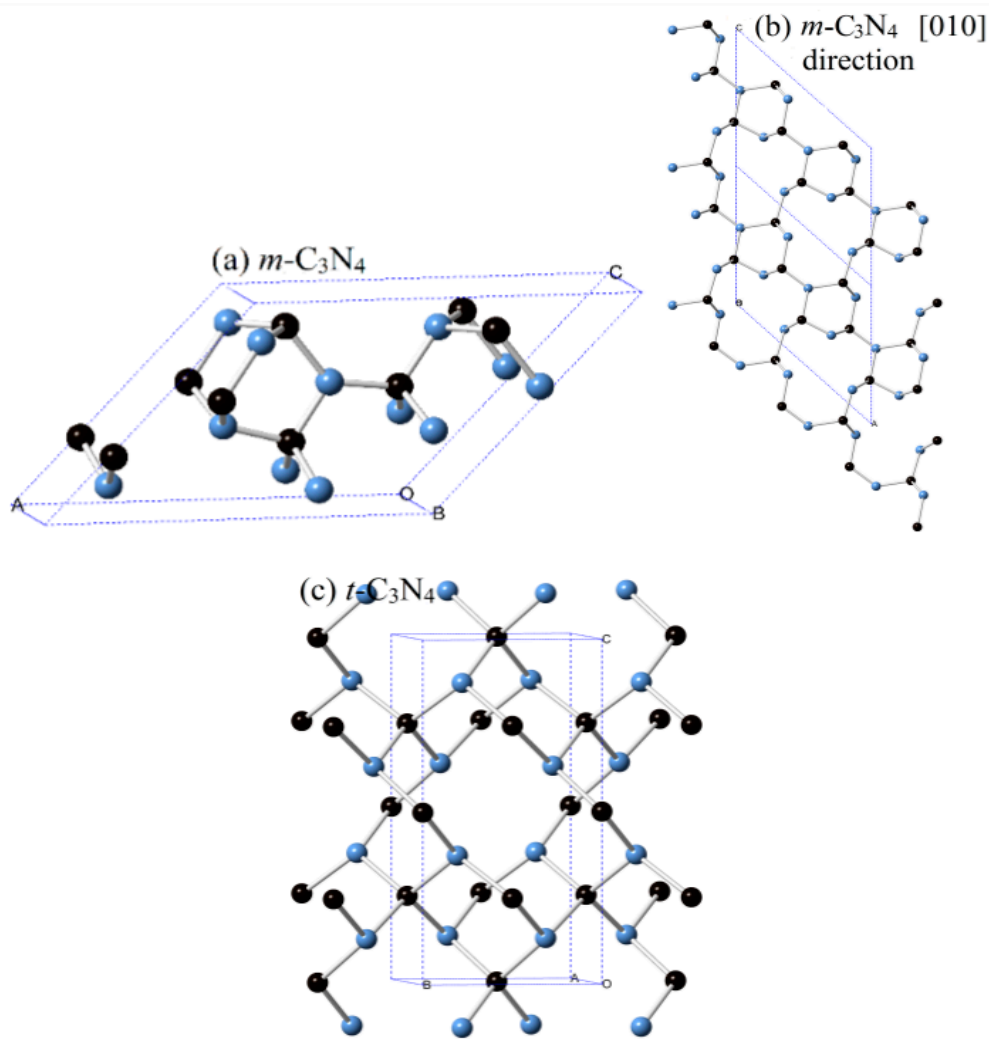


Figure 1. The crystal structures of: $m\text{-C}_3\text{N}_4$ (a,b); and $t\text{-C}_3\text{N}_4$ (c) (black spheres denote carbon atoms, blue spheres denote nitrogen atoms).

Table 1. Calculated lattice parameters (\AA) of $m\text{-C}_3\text{N}_4$, $t\text{-C}_3\text{N}_4$, $d\text{-ZB-C}_3\text{N}_4$, $\text{Cubic-C}_3\text{N}_4$, $\text{Pseudocubic-C}_3\text{N}_4$ and $g\text{-C}_3\text{N}_4$.

Materials	This Work			Other Works
	a	b	c	a, b, c
$\alpha\text{-C}_3\text{N}_4$	6.512	–	4.742	$a = 6.489, c = 4.729$ ^a ; $a = 6.425, c = 4.715$ ^b ; $a = 6.467, c = 4.710$ ^c ; $a = 6.453, c = 4.699$ ^d ; $a = 6.47, c = 4.71$ ^e
$\beta\text{-C}_3\text{N}_4$	6.449	–	2.422	$a = 6.426, c = 2.418$ ^a ; $a = 6.419, c = 2.425$ ^b ; $a = 6.402, c = 2.404$ ^c ; $a = 6.394, c = 2.397$ ^d ; $a = 6.40, c = 2.40$ ^e
$d\text{-ZB-C}_3\text{N}_4$	3.456	–	–	$a = 3.455$ ^f ; $a = 3.52$ ^e ; $a = 3.43$ ^g
$\text{cubic-C}_3\text{N}_4$	5.398	–	–	$a = 5.395\text{--}5.444$ ^h ; $a = 5.40$ ^e
$\text{pseudocubic-C}_3\text{N}_4$	3.456	–	–	$a = 3.41\text{--}3.44$ ^h
$g\text{-C}_3\text{N}_4$	4.791	–	6.769	$a = 4.74, 6.72$ ^e
$m\text{-C}_3\text{N}_4$	8.032	2.418	6.246	–
$t\text{-C}_3\text{N}_4$	3.483	–	6.933	–

^a Reference [37]; ^b Reference [38]; ^c Reference [23]; ^d Reference [39]; ^e Reference [40]; ^f Reference [41]; ^g Reference [22]; ^h Reference [42].

The calculated pressure–volume relationships of m - C_3N_4 and t - C_3N_4 , together with diamond, c -BN, and other C_3N_4 allotropes, are shown in Figure 2. The highest incompressibility along the c -axis is due to m - C_3N_4 in the C_3N_4 allotropes, while along the c -axis, m - C_3N_4 yields the lowest incompressibility at pressures from 0 to 87 GPa; along the b -axis, m - C_3N_4 yields the lowest incompressibility at pressures from 87 to 100 GPa. For the crystal structure, *pseudocubic*- C_3N_4 has the greatest incompressibility in the C_3N_4 allotropes discussed above, while m - C_3N_4 has the weakest incompressibility. However, the incompressibility of t - C_3N_4 is greater than that of c -BN and the incompressibility of m - C_3N_4 is weaker than that of c -BN.

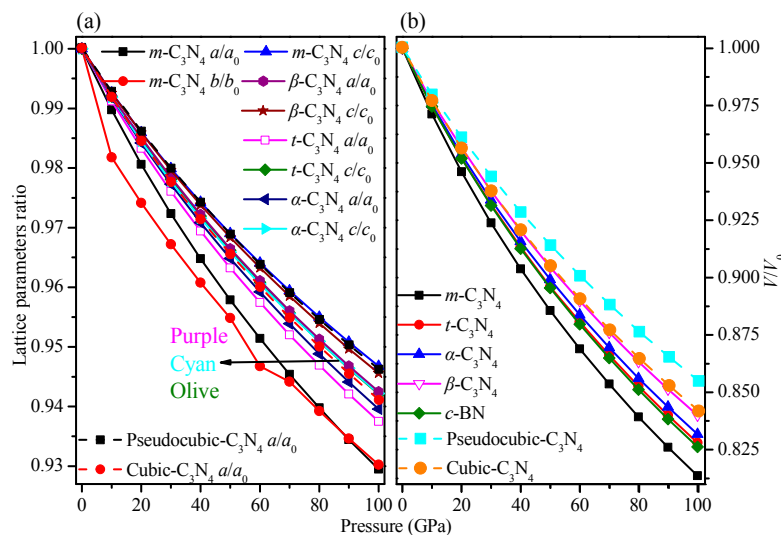


Figure 2. The lattice constants a/a_0 , b/b_0 , c/c_0 and V/V_0 of compression as functions of pressure and temperature for: m - C_3N_4 (a); and t - C_3N_4 (b).

3.2. Elastic Properties and Hardness

In an effort to assess the thermodynamic stability of two novel C_3N_4 allotropes, enthalpy change curves with pressure for various structures were calculated, as presented in Figure 3. The dashed line represents the enthalpy of the summary of diamond and α - N_2 . It can be clearly seen that g - C_3N_4 has the lowest minimum value of enthalpy, which is in good agreement with previous reports and supports the reliability of our calculations [43]. *Pseudocubic*- C_3N_4 has the greatest minimum value of enthalpy. The minimum value of total energy per formula unit of t - C_3N_4 is slightly larger than that of g - C_3N_4 , α - C_3N_4 , m - C_3N_4 , and β - C_3N_4 but much smaller than those of *pseudocubic*- C_3N_4 and *cubic*- C_3N_4 , indicating that t - C_3N_4 and m - C_3N_4 should be thermodynamically metastable phases.

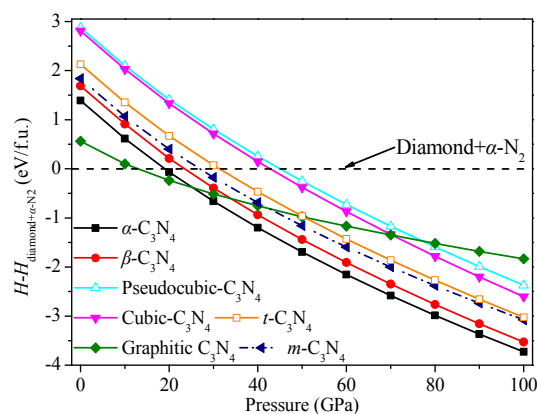


Figure 3. Calculated enthalpies of different C_3N_4 structures relative to diamond and α - N_2 as a function of pressure.

For monoclinic symmetry and tetragonal symmetry, there are different independent elastic constants. Monoclinic symmetry has thirty independent elastic constants (C_{11} , C_{22} , C_{33} , C_{44} , C_{55} , C_{66} , C_{12} , C_{13} , C_{23} , C_{15} , C_{25} , C_{35} and C_{46}), while tetragonal symmetry has six independent elastic constants (C_{11} , C_{33} , C_{44} , C_{66} , C_{12} and C_{13}). The mechanical stability criteria of monoclinic symmetry are given by [44,45]:

$$C_{ii} > 0, i = 1 \sim 6. \quad (1)$$

$$[C_{11} + C_{22} + C_{33} + 2(C_{12} + C_{13} + C_{23})] > 0 \quad (2)$$

$$(C_{33}C_{55} - C_{35}^2) > 0 \quad (3)$$

$$(C_{44}C_{66} - C_{46}^2) > 0 \quad (4)$$

$$(C_{22} + C_{33} - 2C_{23}) > 0 \quad (5)$$

$$[C_{22}(C_{33}C_{55} - C_{35}^2) + 2C_{23}C_{25}C_{35} - C_{23}^2C_{55} - C_{25}^2C_{33}] > 0 \quad (6)$$

$$\begin{aligned} \Omega = & 2[C_{15}C_{25}(C_{33}C_{12} - C_{13}C_{23}) + C_{15}C_{35}(C_{22}C_{13} - C_{12}C_{33}) + \\ & C_{25}C_{35}(C_{11}C_{23} - C_{12}C_{13})] - [C_{15}^2(C_{22}C_{33} - C_{23}^2) + \\ & C_{25}^2(C_{11}C_{33} - C_{13}^2) + C_{35}^2(C_{11}C_{22} - C_{12}^2)] + C_{55}g > 0 \end{aligned} \quad (7)$$

$$g = C_{11}C_{22}C_{33} - C_{11}C_{23}^2 - C_{22}C_{13}^2 - C_{33}C_{12}^2 + 2C_{12}C_{13}C_{23} \quad (8)$$

The criteria for the mechanical stability of tetragonal symmetry are given by [44]:

$$C_{ii} > 0, i = 1, 3, 4, 6. \quad (9)$$

$$(C_{11} - C_{12}) > 0 \quad (10)$$

$$(C_{11} + C_{33} - 2C_{13}) > 0 \quad (11)$$

$$[2(C_{11} + C_{12}) + C_{33} + 4C_{13}] > 0 \quad (12)$$

The calculated elastic constants of α - C_3N_4 , β - C_3N_4 , t - C_3N_4 , d -ZB- C_3N_4 , *pseudocubic*- C_3N_4 , *cubic*- C_3N_4 and m - C_3N_4 are listed in Table 2. Elastic constants under high pressure were also studied. The elastic constants under ambient pressure and high pressure of t - C_3N_4 and m - C_3N_4 satisfied the mechanical stability criteria of monoclinic symmetry and tetragonal symmetry. Namely, t - C_3N_4 and m - C_3N_4 are mechanically stable. To confirm the stability of t - C_3N_4 and m - C_3N_4 , their dynamical stabilities should also be studied under ambient pressure and high pressures. Thus, we calculated the phonon spectra for m - C_3N_4 and t - C_3N_4 at 0 and 100 GPa, as shown in Figure 4. No imaginary frequencies are observed throughout the whole Brillouin zone, signaling dynamically the stabilities of m - C_3N_4 and t - C_3N_4 . The calculated elastic modulus of α - C_3N_4 , β - C_3N_4 , d -ZB- C_3N_4 , *pseudocubic*- C_3N_4 , *cubic*- C_3N_4 , t - C_3N_4 and m - C_3N_4 are listed in Table 3. Bulk modulus B and shear modulus G were calculated by using the Voigt–Reuss–Hill approximation [46–48]. The Voigt and Reuss approximation of monoclinic symmetry is calculated using the following equations [44]:

$$B_V = \frac{1}{9}[C_{11} + C_{22} + C_{33} + 2(C_{12} + C_{13} + C_{23})] \quad (13)$$

$$B_R = \Omega(a + b + c + d + e + f)^{-1} \quad (14)$$

$$a = (C_{33}C_{55} - C_{35}^2)(C_{11} + C_{22} - 2C_{12}) \quad (15)$$

$$b = (C_{23}C_{55} - C_{25}C_{35})(2C_{12} - 2C_{11} - C_{23}) \quad (16)$$

$$c = (C_{13}C_{35} - C_{15}C_{33})(C_{15} - 2C_{25}) \quad (17)$$

$$d = (C_{13}C_{55} - C_{15}C_{35})(2C_{12} + 2C_{23} - C_{13} - 2C_{22}) \quad (18)$$

$$e = (C_{13}C_{25} - C_{15}C_{23})(C_{25} - C_{15}) \quad (19)$$

$$f = C_{11}(C_{22}C_{55} - C_{25}^2) - C_{12}(C_{12}C_{55} - C_{15}C_{25}) + C_{15}(C_{12}C_{25} - C_{15}C_{22}) + C_{25}(C_{23}C_{35} - C_{25}C_{33}) \quad (20)$$

$$G_V = \frac{1}{15}[C_{11} + C_{22} + C_{33} + 3(C_{44} + C_{55} + C_{66}) - (C_{12} + C_{13} + C_{23})] \quad (21)$$

$$G_R = 15 \left\{ \frac{4(f + h + i + j + k + l)}{\Omega} + 3 \left[\frac{g}{\Omega} + \frac{(C_{44} + C_{66})}{C_{44}C_{66} - C_{46}^2} \right] \right\}^{-1} \quad (22)$$

$$h = (C_{33}C_{55} - C_{35}^2)(C_{11} + C_{22} + C_{12}) \quad (23)$$

$$i = (C_{23}C_{55} - C_{25}C_{35})(C_{11} - C_{12} - C_{23}) \quad (24)$$

$$j = (C_{13}C_{35} - C_{15}C_{33})(C_{15} + C_{25}) \quad (25)$$

$$k = (C_{13}C_{55} - C_{15}C_{35})(C_{22} - C_{23} - C_{12} - C_{13}) \quad (26)$$

$$l = (C_{13}C_{25} - C_{15}C_{23})(C_{15} - C_{25}). \quad (27)$$

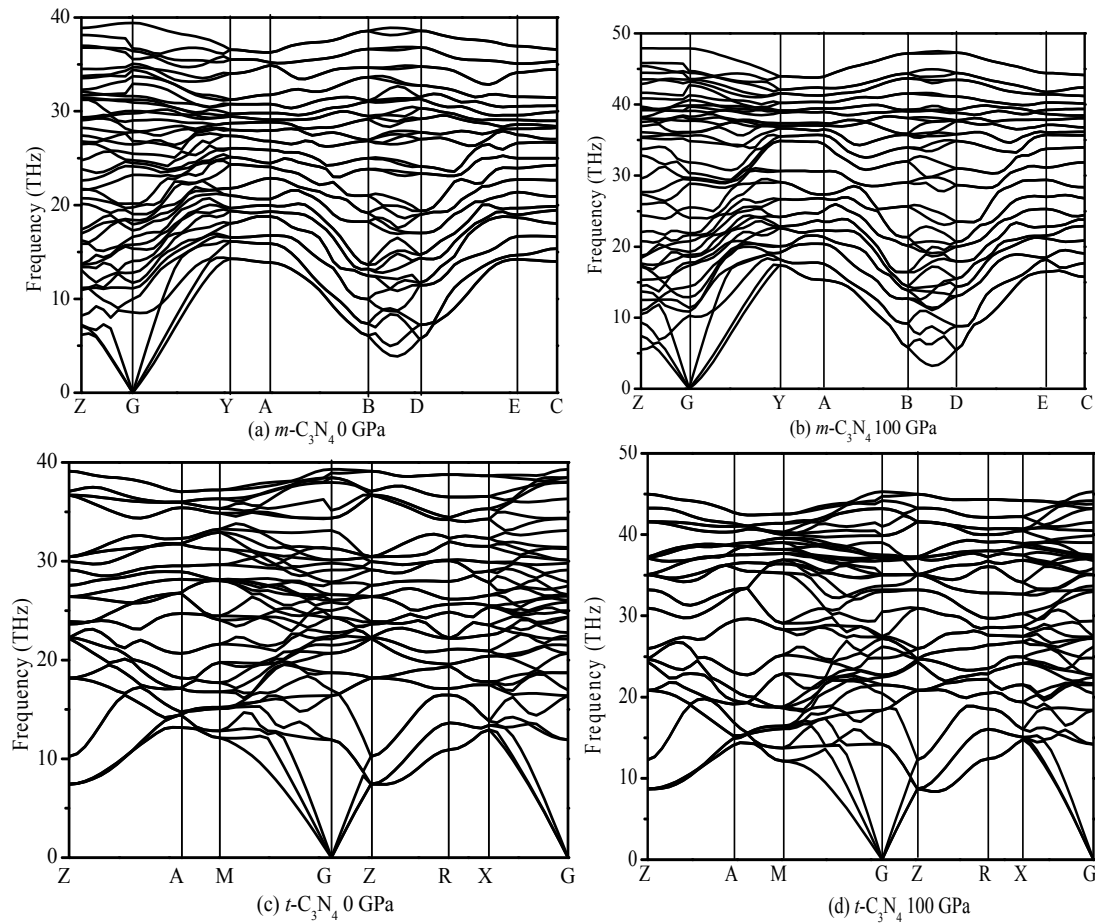


Figure 4. Phonon spectra for: $m\text{-C}_3\text{N}_4$ (a,b); and $t\text{-C}_3\text{N}_4$ (c,d).

The Voigt and Reuss approximation of tetragonal symmetry is calculated using the following equations [44]:

$$B_V = \frac{1}{9}[4C_{13} + C_{33} + 2(C_{11} + C_{12})] \quad (28)$$

$$B_R = \frac{(C_{11} + C_{12})C_{33} - 2C_{13}^2}{C_{11} + C_{12} + 2C_{33} - 4C_{13}} \quad (29)$$

$$G_V = \frac{1}{30}[C_{11} + C_{12} + 2C_{33} - 4C_{13} + 3C_{11} + 12C_{44} + 6C_{66} - 3C_{12}] \quad (30)$$

$$G_R = 15 \left\{ \frac{18B_V}{(C_{11} + C_{12})C_{33} - 2C_{13}^2} + \left[\frac{6}{C_{11} - C_{12}} + \frac{6}{C_{44}} + \frac{3}{C_{66}} \right] \right\}^{-1}. \quad (31)$$

The Hill approximation of monoclinic symmetry and tetragonal symmetry is calculated using the following equation:

$$B_H = \frac{B_V + B_R}{2}, G_H = \frac{G_V + G_R}{2}. \quad (32)$$

Young's modulus and Poisson's ratio can be calculated using the following formulas, respectively: $E = 9B_H G_H / (3B_H + G_H)$, $\nu = (3B_H - 2G_H) / (6B_H + 2G_H)$ [49]. The relationships between elastic constants and pressures are shown in Figure 5a,b. Most of them increase with pressure, whereas C_{66} and C_{15} of $m\text{-C}_3\text{N}_4$ decrease with pressure. The dependence of the elastic constants on pressure of C_{22} of $m\text{-C}_3\text{N}_4$, i.e., $dC_{22}/dP = 6.97$, means that C_{22} of $m\text{-C}_3\text{N}_4$ increases fastest among all elastic constants.

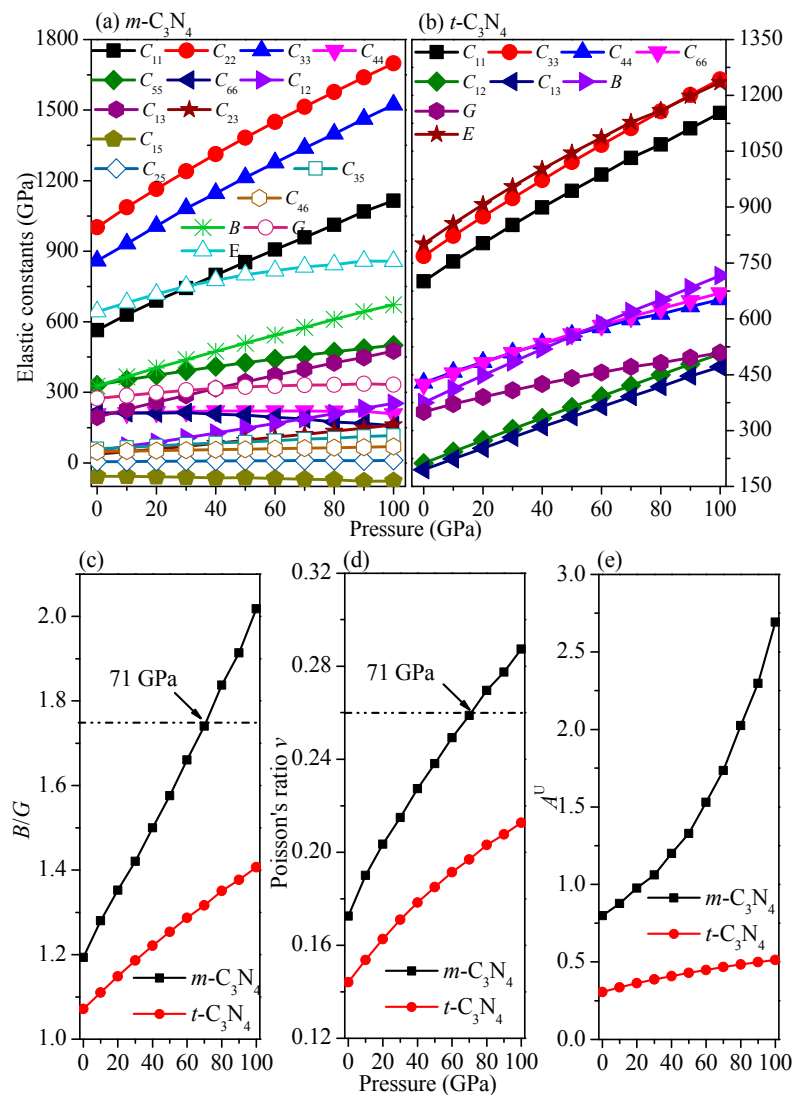


Figure 5. Elastic constants of $m\text{-C}_3\text{N}_4$ (a) and $t\text{-C}_3\text{N}_4$ (b) as a function of pressure, and the ratio B/G (c); Poisson's ratio ν (d); and A^U (e) of $m\text{-C}_3\text{N}_4$ and $t\text{-C}_3\text{N}_4$ as a function of pressure.

Table 2. The calculated elastic constants (GPa) of m -C₃N₄, t -C₃N₄, d -ZB-C₃N₄, $cubic$ -C₃N₄, $pseudocubic$ -C₃N₄ and $cubic$ -BN.

Materials	C ₁₁	C ₂₂	C ₃₃	C ₄₄	C ₅₅	C ₆₆	C ₁₂	C ₁₃	C ₂₃	C ₁₅	C ₂₅	C ₃₅	C ₄₆
α -C ₃ N ₄	848	–	906	319	–	335	179	131	–	–27	–	–	27
Reference [37]	851	–	906	326	–	334	183	129	–	–	–	–	–
β -C ₃ N ₄	852	–	1150	286	–	312	228	111	–	–	–	–	–
Reference [37]	833	–	1049	289	–	287	259	110	–	–	–	–	–
Reference [22]	834	–	1120	305	–	–	279	138	–	–	–	–	–
d -ZB-C ₃ N ₄	791	–	–	443	–	–	184	–	–	–	–	–	–
Reference [41]	794	–	–	431	–	–	184	–	–	–	–	–	–
$Cubic$ -C ₃ N ₄	889	–	–	518	–	–	309	–	–	–	–	–	–
Reference [26]	861	–	–	469	–	–	300	–	–	–	–	–	–
$Pseudocubic$ -C ₃ N ₄	790	–	792	445	–	444	188	187	–	–	–	–	–
Reference [37]	804	–	805	439	–	439	183	183	–	–	–	–	–
m -C ₃ N ₄	564	1002	859	209	331	213	51	195	36	–57	6	60	48
t -C ₃ N ₄	702	–	767	428	–	424	212	195	–	–	–	–	–
$Cubic$ -BN	823	–	–	479	–	–	185	–	–	–	–	–	–
Reference [50]-Exp.	820	–	–	480	–	–	190	–	–	–	–	–	–

Table 3. The calculated elastic modulus (GPa), B/G , hardness Hv (GPa) and the universal anisotropic index of m -C₃N₄, t -C₃N₄, d -ZB-C₃N₄, $cubic$ -C₃N₄, $pseudocubic$ -C₃N₄ and $cubic$ -BN.

Materials	B_V	B_R	G_V	G_R	B_H	G_H	B/G	E	ν	Hv	A^U
α -C ₃ N ₄	386.83	386.82	338.65	335.09	387	337	1.15	784	0.16	78	0.053
Reference [48]	387.60	387.60	341.85	338.96	388	340	1.14	790	0.16	82	0.043
β -C ₃ N ₄	406.11	405.57	330.77	320.96	406	326	1.25	772	0.18	78	0.154
Reference [48]	408.21	407.84	322.09	311.12	408	317	1.29	755	0.19	63, 85 ^a	0.176
d -ZB-C ₃ N ₄	386.59	386.59	387.23	374.16	387	381	1.02	861	0.13	81	0.175
Reference [51]	–	–	–	–	387	375	1.03	850	0.13	63	–
$Cubic$ -C ₃ N ₄	502.48	502.48	426.82	394.18	502	411	1.22	969	0.18	88	0.414
Reference [48]	–	–	–	–	496	401	1.24	948	0.18	90, 87 ^b	–
$Pseudocubic$ -C ₃ N ₄	388.21	388.21	387.66	373.98	388	381	1.02	861	0.13	81	0.183
Reference [48]	390.02	390.02	387.76	376.88	390	382	1.02	864	0.13	70, 80 ^c	0.144
m -C ₃ N ₄	332.22	320.80	293.26	254.44	327	274	1.19	643	0.17	37	0.798
t -C ₃ N ₄	374.81	374.47	360.75	340.05	375	350	1.07	801	0.14	80	0.305
c -BN	397.43	397.43	414.90	398.88	397	407	0.98	910	0.12	63	0.201
–	–	–	–	–	400 ^d	–	–	–	–	66 ^e , 64 ^f	–

^a Reference [52]; ^b Reference [51]; ^c Reference [53]; ^d Reference [50]; ^e Reference [54]; ^f Reference [55].

The dependence of bulk modulus, shear modulus and Young's modulus on pressure of m -C₃N₄ and t -C₃N₄ is 3.49, 0.59, and 2.15 and 3.41, 1.59, and 4.35, respectively. Young's modulus of t -C₃N₄ increases faster than other elastic modulus, while the increase in the shear modulus of m -C₃N₄ is the slowest. At ambient pressure, the bulk modulus of α -C₃N₄, β -C₃N₄, m -C₃N₄ and t -C₃N₄ are 387 GPa, 406 GPa, 327 GPa and 375 GPa, respectively. The calculated hardness of α -C₃N₄, β -C₃N₄, m -C₃N₄, t -C₃N₄, $Cubic$ -C₃N₄, d -ZB-C₃N₄, $Pseudocubic$ -C₃N₄ and c -BN are shown in Table 3. The bulk modulus of t -C₃N₄ is 375 GPa, which is slightly larger than that of c -BN, while the bulk modulus of m -C₃N₄ is slightly smaller than that of c -BN. The hardness of m -C₃N₄ is only 37 GPa, which is approximately half of that of α -C₃N₄, β -C₃N₄, d -ZB-C₃N₄, $pseudocubic$ -C₃N₄ and t -C₃N₄. The reason for this phenomenon is that the mechanical properties of m -C₃N₄ are not excellent compared with the other C₃N₄ allotropes and the bulk modulus, shear modulus and Young's modulus are all smaller than those of other C₃N₄ allotropes.

In materials science, ductility is a solid material's ability to deform under tensile stress. If a material is brittle, when subjected to stress, it will break without significant deformation (strain). Additionally, these material properties are dependent on pressure. Pugh [56] proposed a simple relationship to judge the plastic properties of materials based on their elastic modulus, *i.e.*, B/G . If the ratio B/G is

larger than 1.75, a material exhibits the ductile property; otherwise, the material is brittle. Moreover, Poisson's ratio ν is another criterion for judging the plastic properties of materials [57]. A larger ν value ($\nu > 0.26$) for a material indicates ductility, while a smaller ν value ($\nu < 0.26$) usually denotes brittleness. At ambient pressure, the ratio B/G and ν of α -C₃N₄, β -C₃N₄, d -ZB-C₃N₄, Cubic-C₃N₄, Pseudocubic-C₃N₄, m -C₃N₄ and t -C₃N₄ are as listed in Table 3. The ratio B/G and ν of four C₃N₄ allotropes are all less than 1.75 and 0.26, respectively, which indicates that the four C₃N₄ allotropes are all brittle. t -C₃N₄ has the most brittleness, while β -C₃N₄ has the least brittleness. The pressure dependence of B/G and Poisson's ratio ν are shown in Figure 5c,d, respectively. In Figure 5c,d, the B/G and ν of m -C₃N₄ and t -C₃N₄ increase with increasing pressure. m -C₃N₄ is found to change from brittle to ductile at 71 GPa, while t -C₃N₄ does not change from brittle to ductile in this pressure range.

The elastic anisotropy of a solid is closely related to the possibility of inducing microcracks in materials and can be expressed by the universal anisotropic index (A^U) [58]. The universal anisotropic index is defined as $A^U = 5G_V/G_R + B_V/B_R - 6$. The calculated results of universal anisotropic index are also shown in Table 3. The universal anisotropic index of α -C₃N₄ is only 0.073, which is approximately one-third that of β -C₃N₄, approximately one-sixth that of t -C₃N₄, and approximately one-sixteenth that of m -C₃N₄. Namely, α -C₃N₄ and m -C₃N₄ exhibit the smallest and largest elastic anisotropy in A^U , respectively. The pressure dependence of the universal anisotropic index is shown in Figure 5e. The universal anisotropic index of m -C₃N₄ increases faster than that of t -C₃N₄. The reason for this phenomenon is that the difference between the value of Voigt and Reuss approximations of shear modulus for m -C₃N₄ are greater than that of t -C₃N₄. At 0 GPa (100 GPa), the Voigt approximation values of the shear modulus for m -C₃N₄ and t -C₃N₄ are 293.26 GPa (403.14 GPa) and 360.75 GPa (534.66 GPa), respectively. The Reuss approximation values of the shear modulus for m -C₃N₄ and t -C₃N₄ are 254.44 GPa (262.45 GPa) and 340.05 GPa (484.94 GPa) at 0 GPa (100 GPa), respectively. The difference between the values of the Voigt and Reuss approximations of the shear modulus for m -C₃N₄ ranges from 38.8 to 140.7 GPa at 0 GPa and 100 GPa, respectively. Nevertheless, the difference between the value of the Voigt and Reuss approximations of the shear modulus for t -C₃N₄ only ranges from 20.7 to 49.7 GPa at 0 GPa and 100 GPa, respectively. Thus, the universal anisotropic index m -C₃N₄ increases faster than that of t -C₃N₄.

To analyze the anisotropy of m -C₃N₄ and t -C₃N₄ more systematically, we will investigate the anisotropy of m -C₃N₄ and t -C₃N₄ for Poisson's ratio, the shear modulus and Young's modulus by utilizing the ELAM codes [20,59]. The two-dimensional representations of Poisson's ratio in the xy plane, xz plane and yz plane for m -C₃N₄ and t -C₃N₄ are shown in Figure 6. The blue, red and cyan lines represent Poisson's ratio at 0, 50 and 100 GPa, while the solid line and dash-dot line represent the minimum and maximum values of Poisson's ratio in the xy plane, xz plane and yz plane, respectively. From Figure 6, it is clear that the anisotropy of Poisson's ratio for m -C₃N₄ and t -C₃N₄ increases with increasing pressure. The maximum value of Poisson's ratio for m -C₃N₄ is 0.47, 0.61 and 0.76 at 0, 50 and 100 GPa, while the minimum value of Poisson's ratio for m -C₃N₄ is 0.01; the maximum and minimum values of Poisson's ratio are the same for m -C₃N₄ in the xy plane, xz plane and yz plane. The maximum value of Poisson's ratio for t -C₃N₄ is 0.30, 0.38 and 0.44 at 0, 50 and 100 GPa, respectively, while the minimum value of Poisson's ratio for t -C₃N₄ is 0.0; the maximum and minimum values of Poisson's ratio are the same for t -C₃N₄ in the xy plane, xz plane and yz plane. The difference between the maximum and minimum values of Poisson's ratio for t -C₃N₄ and m -C₃N₄ shows that m -C₃N₄ exhibits greater anisotropy with respect to Poisson's ratio.

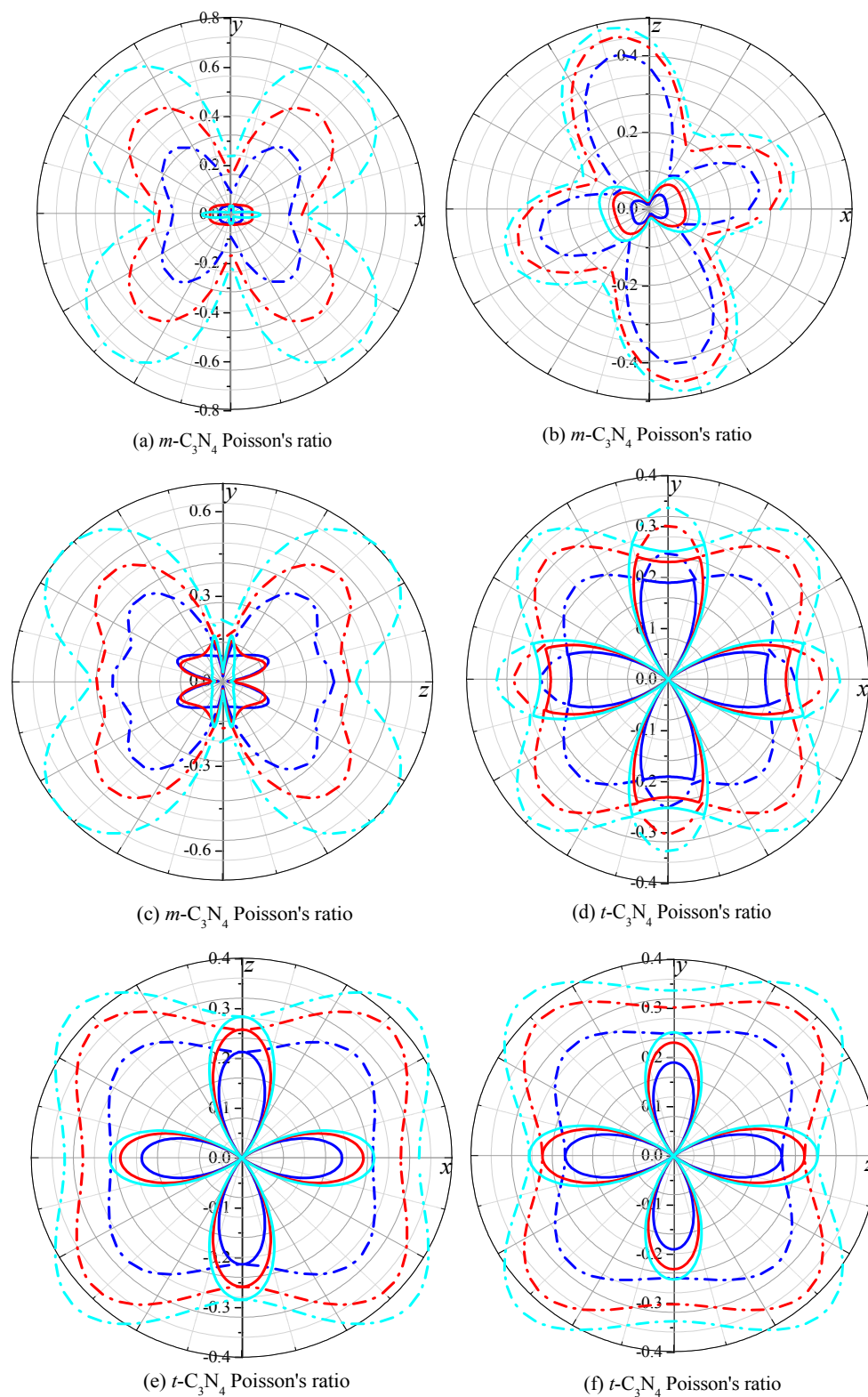


Figure 6. 2D representation of Poisson's ratio in the xy plane, xz plane and yz plane for: $m\text{-C}_3\text{N}_4$ (a–c); and $t\text{-C}_3\text{N}_4$ (d–f). The solid line represents the minimum, and the dashed line represents the maximum. The blue, red and cyan lines represent Poisson's ratio at $p = 0, 50$ and 100 GPa, respectively.

The 2D representations of the shear modulus in the xy plane, xz plane and yz plane for $m\text{-C}_3\text{N}_4$ and $t\text{-C}_3\text{N}_4$ are illustrated in Figure 7. For $m\text{-C}_3\text{N}_4$ in Figure 7a–c, the maximum value of the shear modulus occurs in the deviation from the x axis or y axis of approximately 45 degrees in the xy plane or yz plane, respectively. The maximum value of the shear modulus occurs in the deviation from the x axis or z axis of approximately 15 degrees in the xz plane. Moreover, the minimum value of the shear modulus occurs along the y axis in the xy plane and yz plane, respectively. The maximum and the minimum values of $m\text{-C}_3\text{N}_4$ are 163 GPa and 455 GPa at ambient pressure, respectively, and the ratio $G_{\max}/G_{\min} = 2.79$. At the same time, the maximum and minimum values of $m\text{-C}_3\text{N}_4$ are 153 GPa (110 GPa) and 611 GPa (738 GPa), respectively, at 50 GPa (100 GPa); the ratio $G_{\max}/G_{\min} = 3.99$ at $p = 50$ GPa, and the ratio $G_{\max}/G_{\min} = 6.71$ at $p = 100$ GPa. The anisotropy of $m\text{-C}_3\text{N}_4$ increases with increasing pressure. The average shear modulus of $m\text{-C}_3\text{N}_4$ is 266 GPa, 312 GPa and 328 GPa, respectively. For $t\text{-C}_3\text{N}_4$ in Figure 7d–f, the maximum value of the shear modulus for $t\text{-C}_3\text{N}_4$ in the xy plane, xz plane and yz plane appears along the coordinate axis, while the minimum value of the shear modulus for $t\text{-C}_3\text{N}_4$ in the xy plane, xz plane and yz plane appears in the deviation from the coordinate axis of approximately 45 degrees. The maximum and minimum values of the shear modulus for $t\text{-C}_3\text{N}_4$ are 245 GPa, 291 GPa, 323 GPa and 428 GPa, 559 GPa, 669 GPa at 0 GPa, 50 GPa, 100 GPa, respectively. The ratio $G_{\max}/G_{\min} = 1.75$ at $p = 0$ GPa, the ratio $G_{\max}/G_{\min} = 1.92$ at $p = 50$ GPa, and the ratio $G_{\max}/G_{\min} = 2.07$ at $p = 100$ GPa. It is clear that the ratio G_{\max}/G_{\min} for $t\text{-C}_3\text{N}_4$ is much smaller than that for $m\text{-C}_3\text{N}_4$. In other words, $m\text{-C}_3\text{N}_4$ exhibits greater anisotropy than $t\text{-C}_3\text{N}_4$. This agrees well with our previous prediction of anisotropy with respect to the universal anisotropic index and Poisson's ratio.

As a valid method to describe the elastic anisotropic behavior of a crystal completely, the 3D surface constructions of the directional dependences of reciprocals of Young's modulus are practically useful. The results are shown in Figure 8 for Young's modulus. For an isotropic system, the 3D directional dependence would exhibit a spherical shape, while the deviation degree from the spherical shape reflects the content of anisotropy [60]. In Figure 8a,c, the 3D shape of Young's modulus shows that $m\text{-C}_3\text{N}_4$ exhibits greater anisotropy than $t\text{-C}_3\text{N}_4$. As the pressure increases, the anisotropy of Young's modulus for $m\text{-C}_3\text{N}_4$ and $t\text{-C}_3\text{N}_4$ increases, but $m\text{-C}_3\text{N}_4$ still exhibits greater anisotropy than $t\text{-C}_3\text{N}_4$. To analyze the anisotropy of $m\text{-C}_3\text{N}_4$ and $t\text{-C}_3\text{N}_4$ in detail, the 2D representations of Young's modulus in the xy plane, xz plane and yz plane for $m\text{-C}_3\text{N}_4$ and $t\text{-C}_3\text{N}_4$ are depicted in Figure 9. From Figure 9, it is clear that $m\text{-C}_3\text{N}_4$ has a larger anisotropy and that the anisotropy will become larger with increasing pressure.

Young's modulus of $t\text{-C}_3\text{N}_4$ has the same value in different planes, while that of $m\text{-C}_3\text{N}_4$ has different values in different planes. For example, at ambient pressure, the maximum and minimum values of Young's modulus for $t\text{-C}_3\text{N}_4$ are 928 GPa and 612 GPa in the xy plane, xz plane and yz plane, while at $p = 100$ GPa, they are 1510 GPa and 864 GPa, respectively. However, the maximum value of Young's modulus is 996 GPa in the xy plane and yz plane for $m\text{-C}_3\text{N}_4$, but in the xz plane, it is 995 GPa, and the minimum value is always 476 GPa. At 100 GPa, the difference reaches a larger degree; in the xy plane and yz plane, the maximum value of Young's modulus for $m\text{-C}_3\text{N}_4$ is 1638 GPa, while the maximum value is 1634 GPa. This also proves that $m\text{-C}_3\text{N}_4$ has a larger anisotropy from the other side.

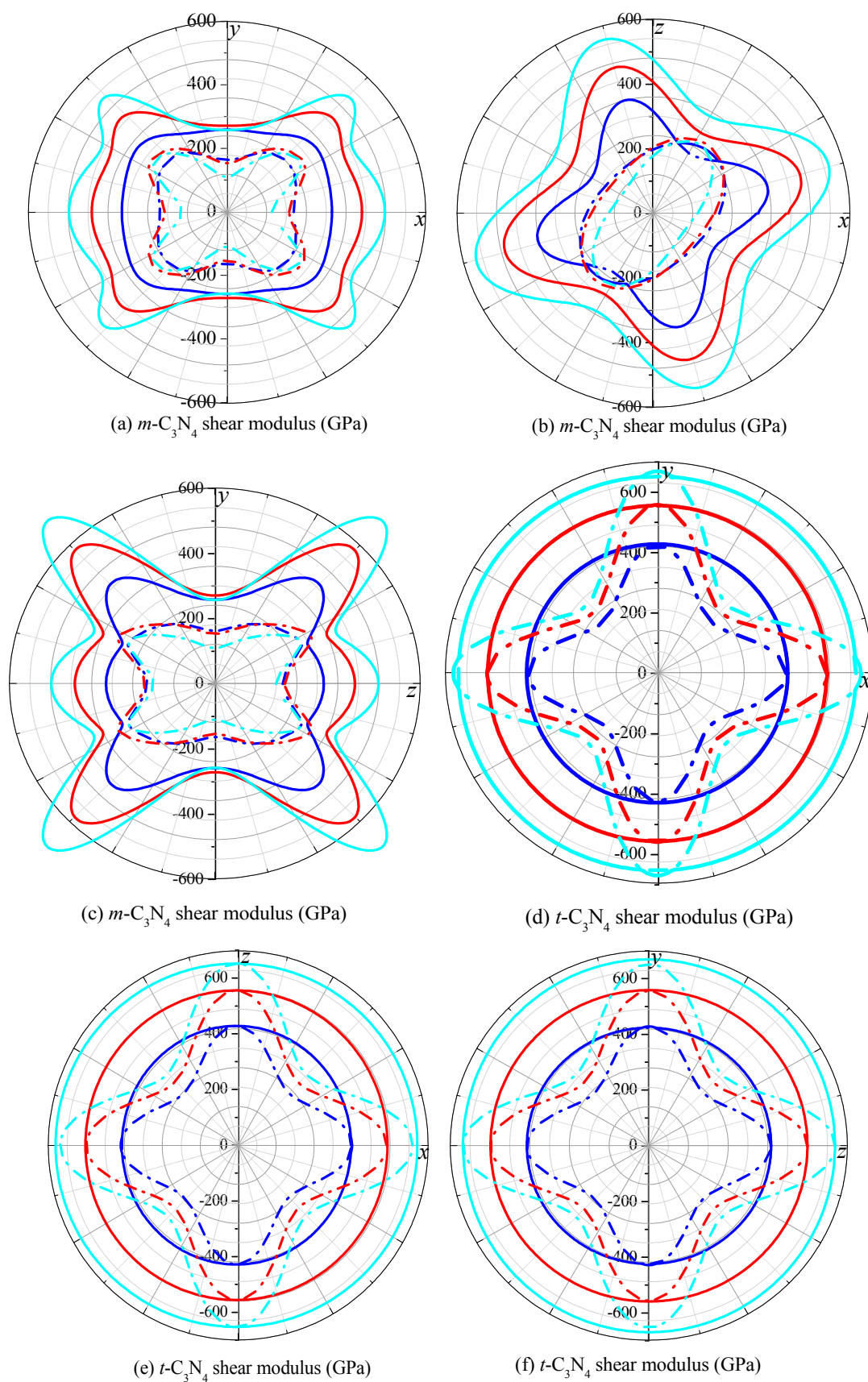


Figure 7. 2D representation of shear modulus in the xy plane, xz plane and yz plane for: $m\text{-C}_3\text{N}_4$ (a–c); and $t\text{-C}_3\text{N}_4$ (d–f).

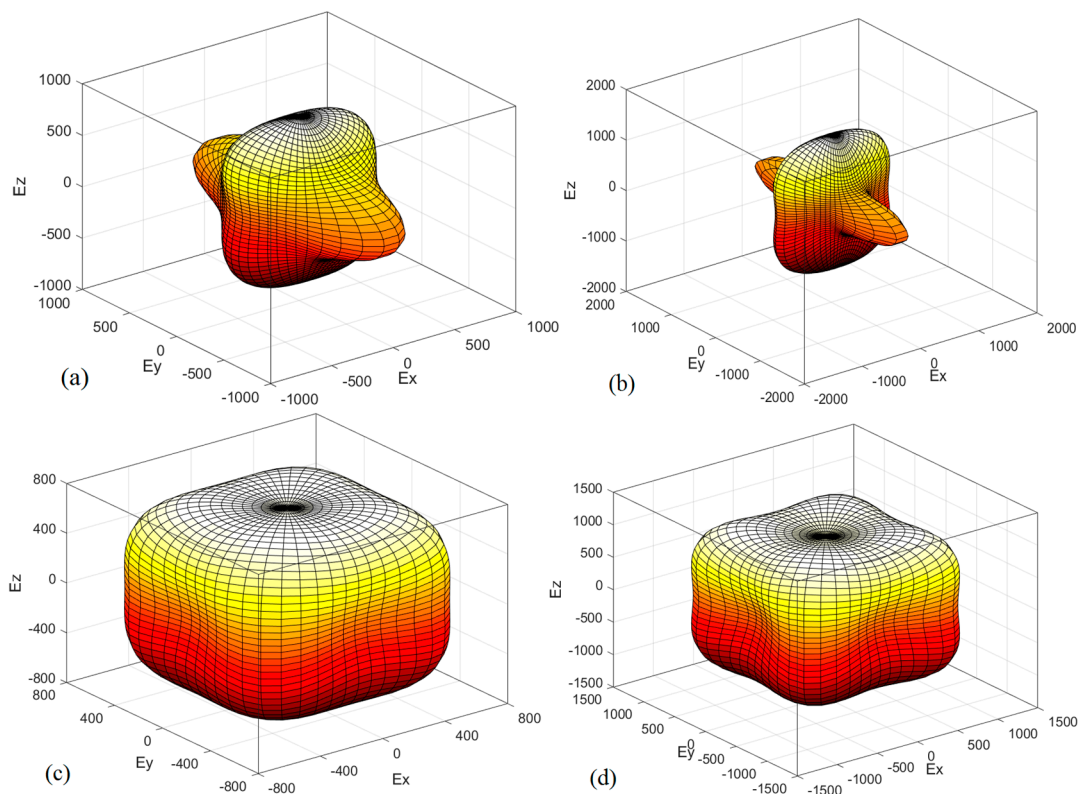


Figure 8. The directional dependence of Young's modulus for: $m\text{-C}_3\text{N}_4$ (a,b); and $t\text{-C}_3\text{N}_4$ (c,d).

3.3. Electronic Structures

Band theory is one of the most stringent tests of the physics of semiconductors. For example, silicon, calcite and copper all contain similar densities of electrons, but they have different physical properties, all inexplicable without quantum mechanics [61]. Thus, it is necessary to understand the band structure and density of states. The band structures and density of states of $m\text{-C}_3\text{N}_4$ and $t\text{-C}_3\text{N}_4$ at different pressures are shown in Figure 10. The band structure calculations show that $m\text{-C}_3\text{N}_4$ is a quasi-direct band gap semiconductor, with a band gap of 4.52 eV (see Figure 10a), and at 100 GPa, $m\text{-C}_3\text{N}_4$ remains a quasi-direct band gap semiconductor, with a band gap of 5.68 eV. $t\text{-C}_3\text{N}_4$ has a quasi-direct band gap of 4.21 eV at (0.322 0.322 0.0) along the M– Γ direction and Γ point, while the direct band gap is 4.22 eV at the Γ point. At 100 GPa, $t\text{-C}_3\text{N}_4$ has a quasi-direct band gap of 4.79 eV at (0.322 0.322 0.0) along the M– Γ direction and Γ point, while the direct band gap is 4.81 eV at the Γ point. At 0 GPa, the valence band maximum (VBM) of $m\text{-C}_3\text{N}_4$ is located at the Z point, the energy of VBM near the Fermi level of $m\text{-C}_3\text{N}_4$ is 10.37 eV, and the energy of the Z point near the Fermi level is 10.39 eV; thus, $m\text{-C}_3\text{N}_4$ is a quasi-direct band gap semiconductor. At 100 GPa, the Fermi level of $m\text{-C}_3\text{N}_4$ increases to 14.04 eV, and the energy of the Z point near the Fermi level of $m\text{-C}_3\text{N}_4$ is 14.02 eV. The VBM of $m\text{-C}_3\text{N}_4$ is located at the point along the Z and Γ directions; its energy is 14.04 eV. The conduction band minimum (CBM) is at the Γ point for $m\text{-C}_3\text{N}_4$ at 0 and 100 GPa. The energy of CBM is 14.91 and 19.72 eV. At 0 GPa, the Fermi level of $m\text{-C}_3\text{N}_4$ is 10.39 eV, which is slightly smaller than that of $t\text{-C}_3\text{N}_4$ (10.52 eV). For $t\text{-C}_3\text{N}_4$, the CBM is at the Γ point for $t\text{-C}_3\text{N}_4$ at 0 and 100 GPa; the energy of CBM is 14.73 and 18.82 eV, respectively. The VBM of $t\text{-C}_3\text{N}_4$ is located at the point along the M and Γ directions; the energy is 10.52 and 14.03 eV, respectively. Moreover, the energy of the Γ point near the Fermi level of $t\text{-C}_3\text{N}_4$ is 10.51 eV and 14.01 eV at 0 and 100 GPa, respectively. Thus, $t\text{-C}_3\text{N}_4$ is a quasi-direct band gap semiconductor. Interestingly, the band gaps of $m\text{-C}_3\text{N}_4$ and $t\text{-C}_3\text{N}_4$ both increase with increasing pressure. At 100 GPa, $m\text{-C}_3\text{N}_4$ increases by 25.61%, and $t\text{-C}_3\text{N}_4$ increases by 13.66% compared with that at 0 GPa.

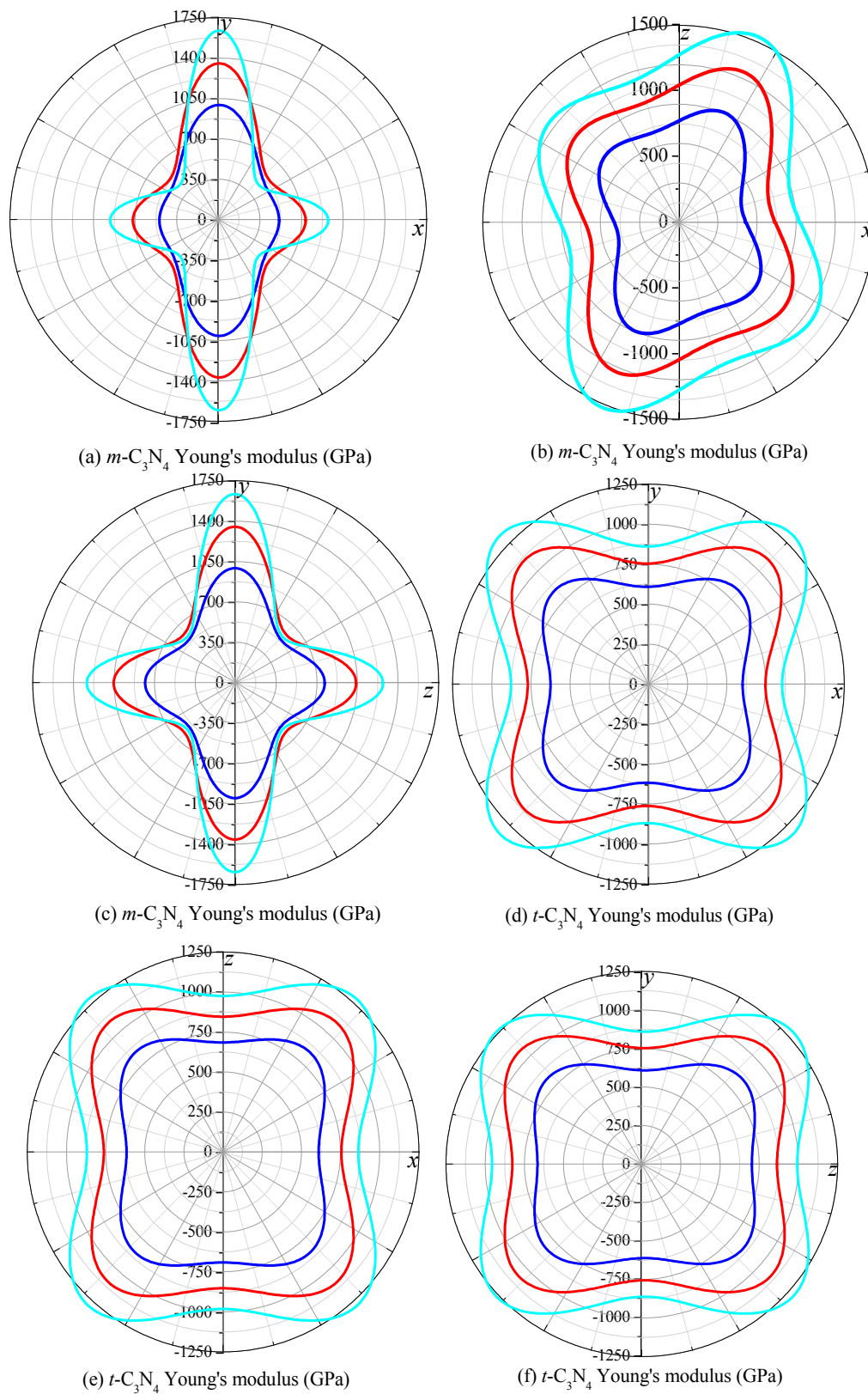


Figure 9. 2D representation of Young's modulus in the xy plane, xz plane and yz plane for: $m\text{-C}_3\text{N}_4$ (a–c); and $t\text{-C}_3\text{N}_4$ (d–f). The blue, red and cyan lines represent Poisson's ratio at $p = 0, 50$ and 100 GPa, respectively.

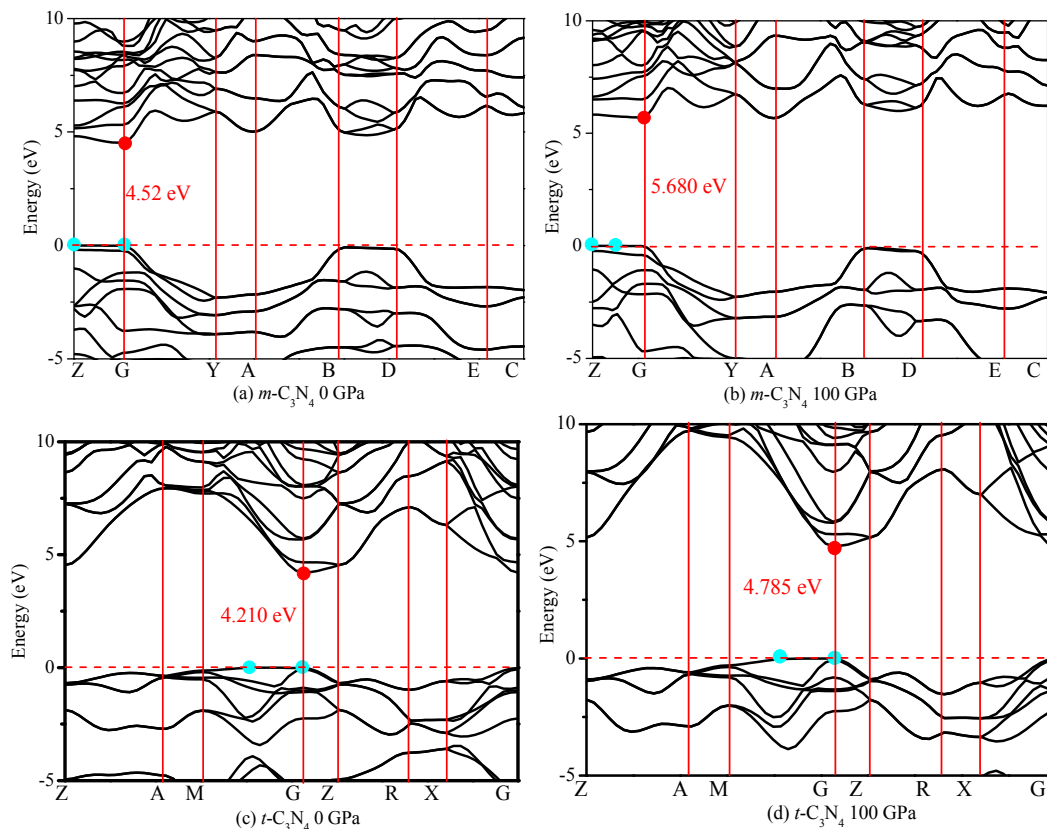


Figure 10. Electronic band structure of: $m\text{-C}_3\text{N}_4$ (a,b); and $t\text{-C}_3\text{N}_4$ (c,d) with HSE06.

4. Conclusions

In conclusion, we have predicted two novel C_3N_4 allotropes, *i.e.*, $m\text{-C}_3\text{N}_4$ and $t\text{-C}_3\text{N}_4$, with space groups Cm and $I-42m$, which are both mechanically and dynamically stable up to at least 100 GPa. The bulk modulus of $t\text{-C}_3\text{N}_4$ is 375 GPa, which is slightly larger than that of $c\text{-BN}$, while the bulk modulus of $m\text{-C}_3\text{N}_4$ is slightly smaller than that of $c\text{-BN}$. The hardness of $t\text{-C}_3\text{N}_4$ is larger than that of $c\text{-BN}$, thereby making it a superhard material with potential technological and industrial applications. The ratio B/G and ν of the two novel C_3N_4 phases are both less than 1.75 and 0.26, respectively, which indicates that the two novel C_3N_4 allotropes are both brittle. The B/G and ν of $m\text{-C}_3\text{N}_4$ and $t\text{-C}_3\text{N}_4$ increase with increasing pressure. $m\text{-C}_3\text{N}_4$ is found to change from being brittle to ductile at 71 GPa, while $t\text{-C}_3\text{N}_4$ does not change from being brittle to ductile in this pressure range. The elastic anisotropy calculations show that $m\text{-C}_3\text{N}_4$ and $t\text{-C}_3\text{N}_4$ both exhibit large anisotropy with respect to Poisson's ratio, the shear modulus and Young's modulus and universal anisotropic index. The band structure calculations show that $m\text{-C}_3\text{N}_4$ and $t\text{-C}_3\text{N}_4$ are a quasi-direct-band-gap semiconductor and a quasi-direct-band-gap semiconductor, respectively. Moreover, the band gaps of $m\text{-C}_3\text{N}_4$ and $t\text{-C}_3\text{N}_4$ continue to be a quasi-direct band-gap and quasi-direct band gap at 100 GPa, respectively. The band gaps of $m\text{-C}_3\text{N}_4$ and $t\text{-C}_3\text{N}_4$ are 4.522 and 4.210 eV, respectively, and these materials are both wide-band-gap semiconductors. Due to their quasi-direct band gaps, they are attractive for luminescent device applications.

Acknowledgments: This work was supported by the Natural Science Foundation of China (No. 61474089), the Natural Science Basic Research plan in Shaanxi Province of China (No. 2016JM1026), and the Open fund of key laboratory of complex electromagnetic environment science and technology, China Academy of Engineering Physics (No. 2015-0214. XY.K).

Author Contributions: Qingyang Fan and Qun Wei designed the project; Qingyang Fan, Changchun Chai and Qun Wei performed the calculations; Qingyang Fan, Qun Wei, and Yintang Yang determined the results; and Qingyang Fan and Changchun Chai wrote the manuscript.

Conflicts of Interest: The authors declare no conflict of interest.

References

1. Hannay, J.B. Artificial Diamonds. *Nature* **1880**, *22*, 255–257. [[CrossRef](#)]
2. Bridgman, P.W. An experimental contribution to the problem of diamond synthesis. *J. Chem. Phys.* **1947**, *15*, 92–98. [[CrossRef](#)]
3. Cote, M.; Cohen, M.L. Carbon nitride compounds with 1:1 stoichiometry. *Phys. Rev. B* **1997**, *55*, 5684–5688.
4. Betranhandy, E.; Matar, S.F. A model study for the breaking of cyanogen out of CN_x within DFT. *Diam. Relat. Mater.* **2006**, *15*, 1609–1613. [[CrossRef](#)]
5. Wang, J.T.; Chen, C.F.; Kawazoe, Y. Orthorhombic carbon allotrope of compressed graphite: *Ab initio* calculations. *Phys. Rev. B* **2012**, *85*, 033410. [[CrossRef](#)]
6. Wang, J.T.; Chen, C.F.; Kawazoe, Y. Low-temperature phase transformation from graphite to sp^3 orthorhombic carbon. *Phys. Rev. Lett.* **2011**, *106*, 075501. [[CrossRef](#)] [[PubMed](#)]
7. Umemoto, K.; Wentzcovitch, R.M.; Saito, S.; Miyake, T. Body-centered tetragonal C_4 : A viable sp^3 carbon allotrope. *Phys. Rev. Lett.* **2010**, *104*, 125504. [[CrossRef](#)] [[PubMed](#)]
8. Li, D.; Bao, K.; Tian, F.B.; Zeng, Z.W.; He, Z.; Liu, B.B.; Cui, T. Lowest enthalpy polymorph of cold-compressed graphite phase. *Phys. Chem. Chem. Phys.* **2012**, *14*, 4347–4350. [[CrossRef](#)] [[PubMed](#)]
9. Li, Q.K.; Sun, Y.; Li, Z.Y.; Zhou, Y. Lonsdaleite—A material stronger and stiffer than diamond. *Scr. Mater.* **2011**, *65*, 229–232.
10. Zhou, R.L.; Zeng, X.C. Polymorphic phases of sp^3 -hybridized carbon under cold compression. *J. Am. Chem. Soc.* **2012**, *134*, 7530–7538. [[CrossRef](#)] [[PubMed](#)]
11. Zhang, M.; Liu, H.Y.; Du, Y.H.; Zhang, X.X.; Wang, Y.C.; Li, Q. Orthorhombic C_{32} : A novel superhard sp^3 carbon allotrope. *Phys. Chem. Chem. Phys.* **2013**, *15*, 14120–14125. [[CrossRef](#)] [[PubMed](#)]
12. He, C.Y.; Sun, L.Z.; Zhang, C.X.; Peng, X.Y.; Zhang, K.W.; Zhong, J.X. New superhard carbon phases between graphite and diamond. *Solid State Commun.* **2012**, *152*, 1560–1563. [[CrossRef](#)]
13. Sheng, X.L.; Yan, Q.B.; Ye, F.; Zheng, Q.R.; Su, G. T-carbon: A novel carbon allotrope. *Phys. Rev. Lett.* **2011**, *106*, 155703. [[CrossRef](#)] [[PubMed](#)]
14. Wei, Q.; Zhang, M.G.; Yan, H.Y.; Lin, Z.Z.; Zhu, X.M. Structural, electronic and mechanical properties of Imma-carbon. *EPL* **2014**, *107*, 27007. [[CrossRef](#)]
15. Cheng, C.; Lv, Z.L.; Cheng, Y.; Chen, X.R.; Cai, L.C. A possible superhard orthorhombic carbon. *Diam. Relat. Mater.* **2014**, *43*, 49–54. [[CrossRef](#)]
16. Wentorf, R.H., Jr. Cubic form of boron nitride. *J. Chem. Phys.* **1957**, *26*, 956. [[CrossRef](#)]
17. Gueorguiev, G.K.; Neidhardt, J.; Stafstrom, S.; Hultman, L. First-principles calculations on the role of CN precursors for the formation of fullerene-like carbon nitride. *Chem. Phys. Lett.* **2005**, *401*, 288–295. [[CrossRef](#)]
18. Gueorguiev, G.K.; Neidhardt, J.; Stafstrom, S.; Hultman, L. First-principles calculations on the curvature evolution and cross-linkage in carbon nitride. *Chem. Phys. Lett.* **2005**, *410*, 228–234. [[CrossRef](#)]
19. Liu, A.Y.; Cohen, M.L. Prediction of new low compressibility solids. *Science* **1989**, *245*, 841–842. [[CrossRef](#)] [[PubMed](#)]
20. Fan, Q.Y.; Wei, Q.; Chai, C.C.; Yan, H.Y.; Zhang, M.G.; Lin, Z.Z.; Zhang, Z.X.; Zhang, J.Q.; Zhang, D.Y. Structural, mechanical, and electronic properties of P3m1-BCN. *J. Phys. Chem. Solids* **2015**, *79*, 89–96. [[CrossRef](#)]
21. Haeuselner, H. X-ray investigations in the system $CdIn_2S_4$ - $CdIn_2Se_4$. *J. Solid State Chem.* **1979**, *29*, 121–123. [[CrossRef](#)]
22. Liu, A.Y.; Wentzcovitch, R.M. Stability of carbon nitride solids. *Phys. Rev. B* **1994**, *50*, 10362. [[CrossRef](#)]
23. Teter, D.M.; Hemley, R.J. Low-compressibility carbon nitrides. *Science* **1996**, *271*, 53–55. [[CrossRef](#)]
24. Mo, S.D.; Ouyang, L.; Ching, W.Y.; Tanaka, I.; Koyama, Y.; Riedel, R. Interesting physical properties of the new spinel phase of Si_3N_4 and C_3N_4 . *Phys. Rev. Lett.* **1999**, *83*, 5046–5049. [[CrossRef](#)]
25. Kroll, P. Pathways to metastable nitride structures. *J. Solid State Chem.* **2003**, *176*, 530–537. [[CrossRef](#)]

26. Manyali, G.S.; Warmbier, R.; Quandt, A.; Lowther, J.E. *Ab initio* study of elastic properties of super hard and graphitic structures of C_3N_4 . *Comput. Mater. Sci.* **2013**, *69*, 299–303. [[CrossRef](#)]
27. Cui, L.; Hu, M.; Wang, Q.Q.; Xu, B.; Yu, D.L.; Liu, Z.Y.; He, J.L. Prediction of novel hard phases of Si_3N_4 : First-principles calculations. *J. Solid State Chem.* **2015**, *228*, 20–26. [[CrossRef](#)]
28. Hohenberg, P.; Kohn, W. Inhomogeneous electron gas. *Phys. Rev.* **1964**, *136*, B864. [[CrossRef](#)]
29. Kohn, W.; Sham, L.J. Self-consistent equations including exchange and correlation effects. *Phys. Rev.* **1965**, *140*, A1133. [[CrossRef](#)]
30. Vanderbilt, D. Soft self-consistent pseudopotentials in a generalized eigenvalue formalism. *Phys. Rev. B* **1990**, *41*, 7892R. [[CrossRef](#)]
31. Clark, S.J.; Segall, M.D.; Pickard, C.J.; Hasnip, P.J.; Probert, M.I.J.; Refson, K.; Payne, M.C. First principles methods using CASTEP. *Z. Kristallogr.* **2005**, *220*, 567–570. [[CrossRef](#)]
32. Perdew, J.P.; Burke, K.; Ernzerhof, M. Generalized gradient approximation made simple. *Phys. Rev. Lett.* **1996**, *77*, 3865. [[CrossRef](#)] [[PubMed](#)]
33. Monkhorst, H.J.; Pack, J.D. Special points for Brillouin-zone integrations. *Phys. Rev. B* **1976**, *13*, 5188. [[CrossRef](#)]
34. Pfrommer, B.G.; Côté, M.; Louie, S.G.; Cohen, M.L. Relaxation of crystals with the quasi-newton method. *J. Comput. Phys.* **1997**, *131*, 233–240. [[CrossRef](#)]
35. Krukau, A.V.; Vydrov, O.A.; Izmaylov, A.F.; Scuseria, G.E. Influence of the exchange screening parameter on the performance of screened hybrid functionals. *J. Chem. Phys.* **2006**, *125*, 224106. [[CrossRef](#)] [[PubMed](#)]
36. Fan, Q.Y.; Chai, C.C.; Wei, Q.; Yang, Y.T. Two novel silicon phases with direct band gaps. *Phys. Chem. Chem. Phys.* **2016**, *18*, 12905–12913. [[CrossRef](#)] [[PubMed](#)]
37. Ruan, L.W.; Xu, G.S.; Chen, H.Y.; Yuan, Y.P.; Jiang, X.; Lu, Y.X.; Zhu, Y.J. The elastic behavior of dense C_3N_4 under high pressure: First-principles calculations. *J. Phys. Chem. Solids* **2014**, *75*, 1324–1333. [[CrossRef](#)]
38. He, D.W.; Zhang, F.X.; Zhang, X.Y.; Qin, Z.C.; Zhang, M.; Liu, R.P.; Xu, Y.F.; Wang, W.K. Synthesis of carbon nitride crystals at high pressures and temperatures. *J. Mater. Res.* **1998**, *13*, 3458–3462. [[CrossRef](#)]
39. Molina, B.; Sansores, L.E. Electronic structure of six phases of C_3N_4 : A theoretical approach. *Mod. Phys. Lett. B* **1999**, *13*, 193. [[CrossRef](#)]
40. Martin-Gil, J.; Martin-Gil, F.J.; Sarikaya, M.; Qian, M.; Jose-Yacamán, M.; Rubio, A. Evidence of a low compressibility carbon nitride with defect-zincblende structure. *J. Appl. Phys.* **1997**, *81*, 2555. [[CrossRef](#)]
41. Tang, X.; Hao, J.; Lia, Y.W. A first-principles study of orthorhombic CN as a potential superhard material. *Phys. Chem. Chem. Phys.* **2015**, *17*, 27821–27825. [[CrossRef](#)] [[PubMed](#)]
42. Goglio, G.; Foy, D.; Demazeau, G. State of Art and recent trends in bulk carbon nitrides synthesis. *Mater. Sci. Eng. R Rep.* **2008**, *58*, 195–227. [[CrossRef](#)]
43. Xu, Y.; Gao, S.P. Band gap of C_3N_4 in the GW approximation. *Int. J. Hydrog. Energy* **2012**, *37*, 11072–11080. [[CrossRef](#)]
44. Wu, Z.J.; Zhao, E.J.; Xiang, H.P.; Hao, X.F.; Liu, X.J.; Meng, J. Crystal structures and elastic properties of superhard IrN_2 and IrN_3 from first principles. *Phys. Rev. B* **2007**, *76*, 054115. [[CrossRef](#)]
45. Fan, Q.Y.; Wei, Q.; Yan, H.Y.; Zhang, M.G.; Zhang, D.Y.; Zhang, J.Q. A New Potential Superhard Phase of OsN_2 . *Acta Phys. Pol. A* **2014**, *126*, 740. [[CrossRef](#)]
46. Voigt, W. *Lehrbuch der Kristallphysik*; Teubner, B.G., Ed.; Johnson Reprint Corp: Leipzig, Germany, 1928.
47. Reuss, A. Berechnung der Fließgrenze von Mischkristallen auf Grund der Plastizitätsbedingung für Einkristalle. *Z. Angew. Math. Mech.* **1929**, *9*, 49–58. [[CrossRef](#)]
48. Hill, R. The elastic behaviour of a crystalline aggregate. *Proc. Phys. Soc. Lond. Sect. A* **1952**, *65*, 349. [[CrossRef](#)]
49. Fan, Q.Y.; Chai, C.C.; Wei, Q.; Yang, Y.T.; Qiao, L.P.; Zhao, Y.B.; Zhou, P.K.; Xing, M.J.; Zhang, J.Q.; Yao, R.H. Mechanical and electronic properties of $Ca_{1-x}Mg_xO$ alloys. *Mater. Sci. Semicond. Process.* **2015**, *40*, 676–684. [[CrossRef](#)]
50. Grimsditch, M.; Zouboulis, E.S.; Polian, A. Elastic constants of boron nitride. *J. Appl. Phys.* **1994**, *76*, 832. [[CrossRef](#)]
51. Levine, J.B.; Nguyen, S.L.; Rasool, H.I.; Wright, J.A.; Brown, S.E.; Kaner, R.B. Preparation and properties of metallic, superhard rhenium diboride crystals. *J. Am. Chem. Soc.* **2008**, *130*, 16953–16958. [[CrossRef](#)] [[PubMed](#)]
52. Zhao, J.; Fan, C. First-principles study on hardness of five polymorphs of C_3N_4 . *Phys. B Condens. Matter* **2008**, *403*, 1956–1959. [[CrossRef](#)]

53. He, J.L.; Guo, L.C.; Guo, X.J.; Liu, R.P.; Tian, Y.J.; Wang, H.T.; Gao, C.X. Predicting hardness of dense C_3N_4 polymorphs. *Appl. Phys. Lett.* **2006**, *88*, 101906. [[CrossRef](#)]
54. Fan, Q.Y.; Wei, Q.; Yan, H.Y.; Zhang, M.G.; Zhang, Z.X.; Zhang, J.Q.; Zhang, D.Y. Elastic and electronic properties of Pbca-BN: First-principles calculations. *Comput. Mater. Sci.* **2014**, *85*, 80–87. [[CrossRef](#)]
55. Huang, Q.; Yu, D.; Zhao, Z.; Fu, S.; Xiong, M.; Wang, Q.; Gao, Y.; Luo, K.; He, J.L.; Tian, Y.J. First-principles study of O-BN: A sp^3 -bonding boron nitride allotrope. *J. Appl. Phys.* **2012**, *112*, 053518. [[CrossRef](#)]
56. Pugh, S.F. XCII. Relations between the elastic moduli and the plastic properties of polycrystalline pure metals. *Lond. Edinb. Dublin Philos. Mag. J. Sci. Ser. 7* **1954**, *45*, 823. [[CrossRef](#)]
57. Duan, Y.H.; Sun, Y.; Peng, M.J.; Zhou, S.G. Anisotropic elastic properties of the Ca–Pb compounds. *J. Alloy. Compd.* **2014**, *595*, 14–21. [[CrossRef](#)]
58. Ranganathan, S.I.; Ostoja-Starzewski, M. Universal elastic anisotropy index. *Phys. Rev. Lett.* **2008**, *101*, 055504. [[CrossRef](#)] [[PubMed](#)]
59. Marmier, A.; Lethbridge, Z.A.D.; Walton, R.I.; Smith, C.W.; Parker, S.C.; Evans, K.E. ElAM: A computer program for the analysis and representation of anisotropic elastic properties. *Comput. Phys. Commun.* **2010**, *181*, 2102–2115. [[CrossRef](#)]
60. Hu, W.C.; Liu, Y.; Li, D.J.; Zeng, X.Q.; Xu, C.S. First-principles study of structural and electronic properties of C_{14} -type Laves phase Al_2Zr and Al_2Hf . *Comput. Mater. Sci.* **2014**, *83*, 27–34. [[CrossRef](#)]
61. Singleton, J. *Band Theory and Electronic Properties of Solids*; Oxford University Press: New York, NY, USA, 2001.



© 2016 by the authors; licensee MDPI, Basel, Switzerland. This article is an open access article distributed under the terms and conditions of the Creative Commons Attribution (CC-BY) license (<http://creativecommons.org/licenses/by/4.0/>).